JFM RAPIDS
journals.cambridge.org/rapids

On the role of the Prandtl number in convection driven by heat sources and sinks

Benjamin Miquel[1],†, Vincent Bouillaut[1], Sébastien Aumaître[1] and Basile Gallet[1]

[1]Université Paris-Saclay, CEA, CNRS, Service de Physique de l'Etat Condensé, 91191 Gif-sur-Yvette, France

We report on a numerical study of turbulent convection driven by a combination of internal heat sources and sinks. Motivated by a recent experimental realisation (Lepot *et al.*, *Proc. Natl Acad. Sci. USA*, vol. 115 (36), 2018, pp. 8937–8941), we focus on the situation where the cooling is uniform, while the internal heating is localised near the bottom boundary, over approximately one tenth of the domain height. We obtain scaling laws $Nu \sim Ra^\gamma Pr^\chi$ for the heat transfer as measured by the Nusselt number Nu expressed as a function of the Rayleigh number Ra and the Prandtl number Pr. After confirming the experimental value $\gamma \approx 1/2$ for the dependence on Ra, we identify several regimes of dependence on Pr. For a stress-free bottom surface and within a range as broad as $Pr \in [0.003, 10]$, we observe the exponent $\chi \approx 1/2$, in agreement with Spiegel's mixing-length theory. For a no-slip bottom surface we observe a transition from $\chi \approx 1/2$ for $Pr \leq 0.04$ to $\chi \approx 1/6$ for $Pr \geq 0.04$, in agreement with scaling predictions by Bouillaut *et al.* (*J. Fluid Mech.* vol. 861, 2019, R5). The latter scaling regime stems from heat accumulation in the stagnant layer adjacent to a no-slip bottom boundary, which we characterise by comparing the local contributions of diffusive and convective thermal fluxes.

Key words: turbulent convection

1. Introduction

Thermal forcing is an important driver for turbulence in numerous natural and industrial flows. Buoyancy greatly impacts the oceanic dynamics of the Earth (Sutherland *et al.* 2019) and of ice-clad moons (Miquel *et al.* 2018; Soderlund 2019), atmospheric flows (Yano, Talagrand & Drossard 2003) and the internal dynamics of planets and stars (Aurnou *et al.* 2015; Guervilly, Cardin & Schaeffer 2019). Implications and consequences range from climate modelling (Plant & Yano 2015) to the generation of magnetic field via the dynamo effect (Browning 2008; Soderlund, King & Aurnou 2012; Calkins *et al.* 2015),

to cite a few. A global characterisation of such convective flows boils down to the critical issue of turbulent heat transport: How is the enhanced heat flux related to the temperature inhomogeneities, the geometry of the system and the properties of the fluid? Owing to the extremely turbulent nature of the natural and industrial flows of interest, one tries to answer the questions above by identifying scaling laws that capture the essential mechanisms at play and are amenable to extrapolations.

Here, we study convection driven by internal sources and sinks (CISS), whose scaling behaviour departs from the standard set-ups of thermal convection, such as Rayleigh–Bénard convection (RBC) (Ahlers, Grossmann & Lohse 2009; Chillà & Schumacher 2012), horizontal convection (HC) (Vreugdenhil, Griffiths & Gayen 2017; Rocha *et al.* 2020) or even internally heated convection with a cooling top surface (Goluskin 2015) or between fixed-temperature plates (Goluskin & van der Poel 2016). Indeed, the latter set-ups all display thermal boundary layers that greatly throttle the heat flux, whereas these boundary layers are bypassed in CISS, which results in a more efficient heat-transport scaling regime. For instance, a recent experimental and numerical study of CISS in water by Lepot, Aumaître & Gallet (2018) investigated the dependence of the heat flux with the temperature difference in the fluid. The dimensionless counterpart to this question amounts to finding a relationship between the standard Nusselt number and Rayleigh number (see (2.3) for definitions). Lepot *et al.* (2018) measured $Nu \sim Ra^{\gamma}$ with $\gamma \approx 0.5$. This is in strong contrast with RBC experiments and numerical studies where $0.27 \leq \gamma \leq 0.39$ (Castaing *et al.* 1989; Chavanne *et al.* 1997; Niemela *et al.* 2000; Ahlers *et al.* 2009; He *et al.* 2012; Doering, Toppaladoddi & Wettlaufer 2019). This range of measured exponents support the fact that diffusivity coefficients play a role in the RBC set-up, through the formation of boundary layers that throttle the heat flux.

The scope of the present study is to investigate the variation of the heat flux as the Prandtl number (defined as the ratio of the fluid diffusivity coefficients, see (2.2)) varies. Even for the much studied RBC case, such studies remain scarce. In the laboratory, low Prandtl numbers are reached by employing liquid metal (Fauve, Laroche & Libchaber 1981; Cioni, Ciliberto & Sommeria 1997; Aurnou *et al.* 2018), which severely hinders measurements and virtually forbids visualisations. Direct numerical simulations (DNS) exhibit much more flexibility from the standpoint of diffusivity coefficients and have proved invaluable for understanding the role on the Prandtl number for both RBC (Shishkina *et al.* 2017) and HC (Shishkina & Wagner 2016). In the present study, we employ DNS to explore the parameter space of CISS. In particular, we scrutinise recent predictions by Bouillaut *et al.* (2019) that not only provide a model for the experimental results of Lepot *et al.* (2018), but also predict two distinct regimes characterised by different scaling behaviours with respect to the Prandtl number.

The paper is laid out as follows. The formulation of the governing equations and the numerical methods are presented in § 2. Models for the heat transfer law are presented in § 3 and the existence of two different regimes is predicted, depending on the Prandtl number. These regimes are evidenced in a data set obtained from DNS and presented in § 4, together with an analysis of the thermal boundary layers. Finally, § 5 contains a discussion and closing remarks.

2. Governing equations and numerical procedure

2.1. *Model and parameters*

We consider a horizontal fluid layer of depth H, kinematic viscosity ν, thermal diffusivity κ, specific heat capacity C_p and thermal expansion coefficient α, all of which are

considered constant. The layer is subjected to the vertical gravitational acceleration of (uniform) magnitude g. We consider the Boussinesq approximation, where the density ρ is constant and uniform, except in the expression of the buoyancy force. Volumic heat sources and sinks are present in the bulk of the fluid. In the experiment by Lepot *et al.* (2018) and Bouillaut *et al.* (2019), a powerful spotlight shines visible light through the transparent bottom of the tank, into dyed water where absorption occurs over a typical length ℓ. Following Beer–Lambert's law, the intensity of light decreases exponentially with the height Z, measured from the bottom surface. Thus, we model the experimental radiation-induced heating with an exponentially decreasing volumic heat source in the present numerical work

$$Q_L(Z) = \frac{P}{\ell} \frac{\exp\left(-Z/\ell\right)}{1 - \exp\left(-H/\ell\right)}, \tag{2.1}$$

where P is the incident light flux at the bottom of the tank (power per unit area), which gets deposited into the fluid through absorption. In the laboratory experiment, this internal heat source yields 'secular heating' of the fluid, which amounts to a quasi-stationary state with homogeneous internal cooling $Q_c(Z) = P/H$ balancing the radiative heat input, so that the net power deposited in the fluid layer vanishes: $\int_0^H (Q_L(Z) - Q_c(Z))\,\mathrm{d}Z = 0$. We stress the fact that, motivated by the experimental realisations, we are concerned with a distribution of heat sources that takes on finite values at the boundaries. In that respect, the problem of interest here crucially differs from previous studies by Barker, Dempsey & Lithwick (2014), who consider a distribution of heat sources and sinks that vanishes at the boundaries.

The characteristics of the set-up can be cast into three dimensionless control parameters, namely the Prandtl number Pr, the flux-based Rayleigh number Ra_Q and the dimensionless light absorption length $\tilde{\ell}$

$$Pr = \frac{\nu}{\kappa}, \quad Ra_Q = \frac{\alpha g P H^4}{\rho C_p \kappa^2 \nu}, \quad \tilde{\ell} = \frac{\ell}{H}. \tag{2.2a–c}$$

The response of the fluid to the imposed flux may be characterised by the magnitude of the temperature difference ΔT that appears between the bottom plate $(Z = 0)$ and mid-depth $(Z = H/2)$, and the characteristic flow velocity U. To make contact with the numerous RBC literature, one can then define the Reynolds number Re, the temperature-based Rayleigh number Ra and the Nusselt number Nu

$$Re = \frac{UH}{\nu}, \quad Ra = \frac{\alpha g \Delta T H^3}{\nu \kappa}, \quad Nu = \frac{PH}{\rho C_p \kappa \Delta T}, \quad \text{with } Ra_Q = Ra\,Nu. \tag{2.3a–c}$$

2.2. *Dimensionless equations and parameters*

The Boussinesq equations are written in a dimensionless form by counting lengths in units of the depth H, time in units of diffusive time H^2/κ and temperature in units of $\nu\kappa/\alpha g H^3$. Thus, the governing equations for the solenoidal velocity field $(\nabla \cdot \boldsymbol{u} = 0)$ and temperature field θ are

$$Pr^{-1}\left(\partial_t \boldsymbol{u} + \boldsymbol{u} \cdot \nabla \boldsymbol{u}\right) = -\nabla p + \theta\,\hat{\boldsymbol{e}}_z + \nabla^2 \boldsymbol{u}, \tag{2.4a}$$

$$\partial_t \theta + \boldsymbol{u} \cdot \nabla \theta = \nabla^2 \theta + Ra_Q \left(\frac{\exp\left(-z/\tilde{\ell}\right)}{\tilde{\ell}\left[1 - \exp\left(-1/\tilde{\ell}\right)\right]} - 1\right), \tag{2.4b}$$

900 R1-3

where $z = Z/H$. These governing equations are supplemented with adiabatic boundary conditions for temperature: $\partial_z \theta = 0$ at $z = 0, 1$. Kinematic boundary conditions are always impenetrable ($w = 0$) and either no slip ($u = v = 0$) or stress free ($\partial_z u = \partial_z v = 0$) at the top and bottom. Finally, we consider periodic boundary conditions in the horizontal.

2.3. *Numerical procedure*

Direct numerical simulations of equations (2.4) are performed with the High-Performance-Computing code *Coral*, which employs a Chebyshev–Fourier–Fourier decomposition in space and a family of implicit–explicit time-stepping schemes. The boundary conditions in the vertical direction z are enforced using Galerkin basis recombination. Computations are initialised with either small-amplitude noise or a previous solution and are carried out until a statistically stationary regime is clearly identified. *Coral* was already used for studying CISS in Miquel *et al.* (2019), where it is benchmarked against analytical solutions. The non-periodic version of *Coral* has also been benchmarked against the numerical solutions obtained by Lepot *et al.* (2018) using the solver *Dedalus* (Burns *et al.* 2020), for $Pr = 1$ and 7.

3. Scaling arguments

For completeness, we recall in broad strokes the scalings predicted by Bouillaut *et al.* (2019). Experiments and numerical simulations indicate that the large-scale flow consists of turbulent convection cells of aspect ratio close to one, the velocity of which obeys the free-fall scaling law $U \sim \sqrt{\alpha g \Delta T H}$.

3.1. *Bulk transport*

As a fluid element circles around a turbulent convection cell, it rapidly heats up in the region $z \lesssim \tilde{\ell}$, while it slowly cools down in the region $z \gtrsim \tilde{\ell}$. In other words, the heat input inside the region $z \lesssim \tilde{\ell}$ is carried outside the heating region by the flow, which amounts to a balance between the source term and the horizontal advection term in the heat equation

$$\rho C_p U \partial_x T \sim \frac{P}{\ell}. \tag{3.1}$$

Upon inserting the free-fall velocity estimate, the balance above yields an estimate ΔT_{bulk} for the temperature difference between the heating region $z \lesssim \tilde{\ell}$ and the bulk region $z \gtrsim \tilde{\ell}$. In dimensional and dimensionless form:

$$(\Delta T_{bulk})^3 \sim \frac{P^2 H}{\alpha g \rho^2 C_p^2 \ell^2}, \quad Nu \sim \tilde{\ell}\sqrt{RaPr}. \tag{3.2a,b}$$

The reasoning above and the associated ΔT_{bulk} do not take into account the velocity boundary conditions at the bottom plate. In the next section, we show that the latter can induce a possibly stronger temperature difference ΔT_{BL} between the immediate vicinity of the bottom boundary and the heating region $z \lesssim \tilde{\ell}$. The total temperature difference between the bottom plate and the bulk region $z \gtrsim \tilde{\ell}$ is then estimated as $\Delta T = \Delta T_{BL} + \Delta T_{bulk}$.

900 R1-4

3.2. *Stagnant layers near no-slip boundaries*

The scaling law (3.2) may be modified in the case of a no-slip bottom boundary condition. Indeed, the stagnant layer in the immediate vicinity of the bottom plate accumulates heat, and without efficient advection outside this region, the heat can only be diffused away. This leads to a thermal boundary layer of thickness δ_Θ. Balancing the heat source term with the diffusive one estimated inside the boundary layer leads to

$$\rho C_p \kappa \frac{\Delta T_{BL}}{\delta_\Theta^2} \sim \frac{P}{\ell}, \tag{3.3a}$$

yielding

$$\Delta T_{BL} = \frac{PH^2}{\rho C_p \kappa \ell} \frac{\delta_\Theta^2}{H^2}. \tag{3.3b}$$

A final relation between the Nusselt number and the Rayleigh and Prandtl numbers is obtained by supplementing (3.3) with a scaling estimate of the boundary-layer thickness δ_Θ. The latter depends crucially on the Prandtl number: in the case of low Prandtl fluids, a naive laminar estimate would lead to a thermal boundary layer thicker than the kinematic one. However, one expects vigorous turbulent mixing outside the kinematic boundary layer, so that both boundary layers end up having the same thickness. We obtain $\delta_\Theta \sim H/\sqrt{Re}$. Upon estimating the Reynolds number using the free-fall velocity scaling (based on ΔT_{BL} in a worst-case scenario), equation (3.3) becomes

$$(\Delta T_{BL})^3 \sim \frac{P^2 H}{\alpha g \rho^2 C_p^2 \ell^2} \frac{\nu^2}{\kappa^2}, \tag{3.4}$$

which remains negligible compared with the bulk temperature jump from equation (3.2) when $Pr \ll 1$. As a consequence, the scaling law $Nu \sim \tilde{\ell}\sqrt{RaPr}$ remains valid and is not modified by the stagnant bottom layer for $Pr \ll 1$.

The situation is crucially different for high Prandtl fluids. The thermal boundary layer is much thinner than, and nested into, the kinetic one. The flow in the vicinity of the no-slip bottom surface is perceived by the thermal boundary layer as a parallel shear flow, the bottom shear $S(0)$ being estimated as $S(0) \sim U/\delta_\nu \sim U\sqrt{Re}/H \sim \sqrt{U^3/H\nu}$. The boundary-layer thickness is set by a balance between slow advection by the shear , at a speed $S(0)\delta_\Theta$, and vertical diffusion

$$\rho C_p S(0)\delta_\Theta \frac{\Delta T_{BL}}{H} \sim \frac{\rho C_p \kappa \Delta T_{BL}}{\delta_\Theta^2}, \tag{3.5a}$$

so that

$$\frac{\delta_\Theta}{H} \sim \left(\frac{\kappa}{S(0)H^2}\right)^{1/3} \sim \frac{1}{Re^{1/2} Pr^{1/3}}. \tag{3.5b}$$

Inserting this expression for the thermal boundary-layer thickness into equation (3.3), one gets the temperature jump associated with the sheared thermal layer and the associated dimensionless heat flux

$$(\Delta T_{BL})^3 \sim \frac{P^2 H}{\alpha g \rho^2 C_p^2 \ell^2} \left(\frac{\nu}{\kappa}\right)^{2/3}, \quad Nu \sim \tilde{\ell}Ra^{1/2}Pr^{1/6}. \tag{3.6a,b}$$

Noticeably, a comparison with equation (3.2) informs us that the temperature jump in the stagnant boundary layer dominates the temperature jump in the bulk: $\Delta T \simeq \Delta T_{BL}$ when

900 R1-5

$Pr \gg 1$. This observation results in a modification of the Nusselt number scaling law due to boundary-layer corrections, see equation (3.6).

The last case that requires our attention is the case of high Prandtl number flows with a stress-free bottom surface. Within the thermal boundary layer, the flow is well approximated by a uniform parallel flow with velocity $U \sim \sqrt{\alpha g \Delta T_{BL} H}$. Here, in view of finding hypothetical boundary-layer corrections, we assume again that the overall temperature difference is dominated by the contribution from the boundary layer ΔT_{BL}, before testing this assumption *a posteriori*. A triple balance between horizontal advection, diffusion through the layer and heating yields

$$\rho C_p \sqrt{\alpha g \Delta T_{BL} H} \frac{\Delta T_{BL}}{H} \sim \rho C_p \kappa \frac{\Delta T_{BL}}{\delta_{\Theta}^2} \sim \frac{P}{\ell}. \qquad (3.7)$$

This balance is similar to the bulk balance (3.1). Some straightforward algebra confirms that a transport law identical to (3.2) is found. We conclude that no boundary-layer-induced corrections to the heat-transport scaling law are necessary in this case.

To summarise, the scaling theory results in the following predictions for the dimensionless heat flux:

$$Nu = \begin{cases} c_1 \tilde{\ell} \sqrt{RaPr} & \text{with stress-free b. c.,} & \forall Pr, \\ c_2 \tilde{\ell} \sqrt{RaPr} & \text{with no-slip b. c.,} & Pr \ll Pr_*, \\ c_3 \tilde{\ell} Ra^{1/2} Pr^{1/6} & \text{with no-slip b. c.,} & Pr \gg Pr_*, \end{cases} \qquad (3.8)$$

where the dimensionless prefactors c_i remain to be determined. The transition Prandtl number Pr_* is estimated by equating the two no-slip predictions at $Pr = Pr_*$, which yields $Pr_* = (c_3/c_2)^3$.

4. Observations of the two regimes

We now turn to an extensive numerical study, with the goal of (i) assessing the validity of the scaling predictions (3.8), (ii) estimating the transition Prandtl number Pr_* and (iii) determining the dimensionless prefactors c_i, so that (3.8) can be used as a quantitative relation in cases of practical interest. Throughout this section, the dimensionless absorption length is set to $\tilde{\ell} = 0.1$. The domain is cubic with periodic boundary conditions in the horizontal and with insulated top and bottom boundaries. The top boundary condition is always no slip, and the bottom one is either stress free or no slip.

4.1. *Heat flux scalings*

Guided by the prediction (3.8) and the observations by Lepot *et al.* (2018) for $Pr = 1$ and 7, we represent in figure 1(*a*) the Nusselt number Nu compensated by $\sqrt{Ra}$ for data obtained in a suite of DNS runs with almost logarithmically equispaced Prandtl number values: $Pr \in \{0.003, 0.01, 0.03, 0.1, 0.3, 1, 3, 10\}$. We observe that, for a fixed Prandtl number (a given colour on the figure), the data form a plateau as the thermal forcing Ra_Q varies. This confirms that the scaling exponent $\gamma = 0.5$ is universal and does not depend on the Prandtl number, in line with prediction (3.8).

We now turn to the central question of this paper – the Prandtl number dependence – which amounts to analysing the height of the plateaus in figure 1(*a*). In this logarithmic
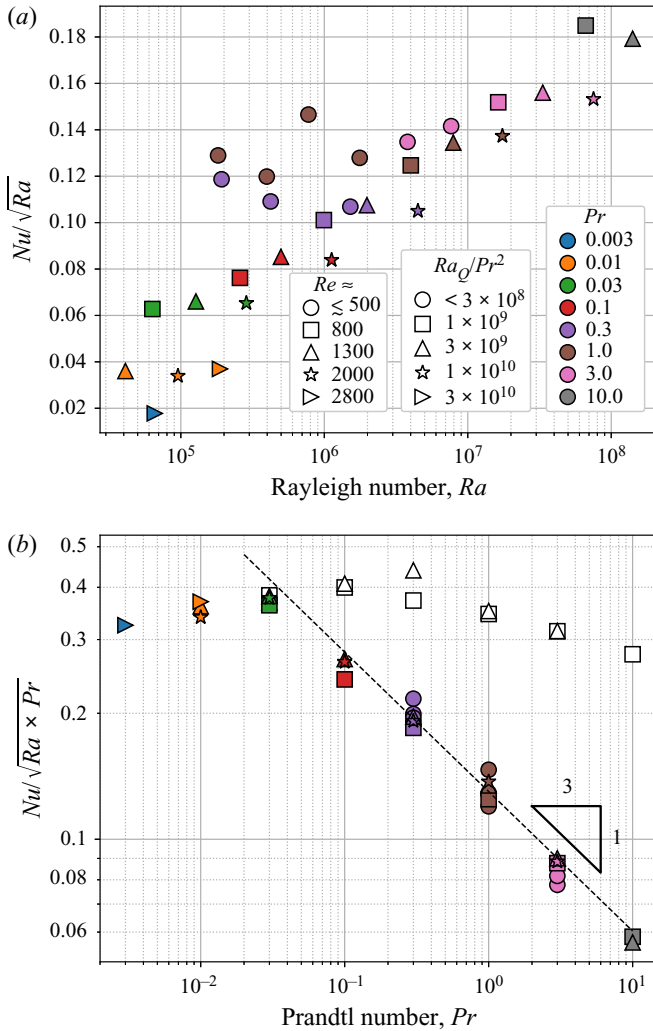
FIGURE 1. (a) Compensated heat flux $Nu/\sqrt{Ra}$ as a function of the Rayleigh number Ra for no-slip boundary conditions. The colour code is for the Prandtl number Pr, while the heating intensity as measured by Ra_Q/Pr^2 is encoded in the shape of the symbols. For convenience, we provide a correspondence between the parameter Ra_Q/Pr^2 and the Reynolds number Re. This colour/shape code is employed consistently thereafter throughout the paper. (b) Compensated heat flux $Nu/\sqrt{RaPr}$ as a function of Pr for no-slip (filled symbols) and stress-free (open symbols) bottom boundaries.

representation, the plateaus are separated by a distance that seems to vary with the Prandtl number.

To better characterise this effect, we turn to figure 1(b) where we plot the heat flux compensated by $\sqrt{RaPr}$ – the scaling prediction (3.8) in the absence of boundary-layer correction – as a function of the Prandtl number. Upon this rescaling, the data points for no-slip boundary conditions (filled symbols) fall on a master curve that exhibits: (i) a plateau for $Pr \lesssim 0.04$, providing evidence for the $Nu \sim \sqrt{RaPr}$ scaling at low Prandtl numbers; (ii) a scaling law with slope $-1/3$ for $Pr \gtrsim 0.04$ which, when combined with

FIGURE 2. (*a*) Temperature profiles averaged in time and along horizontal directions x and y, for $Pr = 3$, $Ra_Q = 3 \times 10^{10}$, with either a no-slip (blue) or a stress-free (orange) bottom boundary. (*b*) Time and horizontally averaged contributions to the total heat flux. Solid lines represent the diffusive flux $-\overline{\partial_z \theta}$, whereas dashed lines represent the convective flux $\overline{w\theta}$. Coloured circles materialise z_{max}, the altitude where the diffusive flux is maximum. For a no-slip bottom boundary (top panel), the thin horizontal black line represents the altitude z_* where the diffusive and the convective fluxes are equal (see text).

the rescaling of the figure, suggests the $Nu \sim Ra^{1/2}Pr^{1/6}$ scaling predicted at high Prandtl numbers.

By contrast, the data points obtained for stress-free boundary conditions (open symbols) reasonably form a plateau, as they exhibit variations of less than 30 % when Pr spans three and a half decades. This observation validates the mixing-length scaling $Nu \sim \sqrt{RaPr}$ at all Prandtl numbers for stress-free boundary conditions.

To summarise, the numerical data are fully compatible with the prediction (3.8), with the following values for the dimensionless prefactors and transition Prandtl number: $c_1 = c_2 \simeq 0.38$, $c_3 \simeq 0.13$, which leads to $Pr_* = (c_3/c_2)^3 \simeq 0.04$.

4.2. *Boundary-layer structure: no-slip case*

We have established that, in the high Prandtl number regime $Pr \gtrsim 0.04$, thermal transfer laws differ for a no-slip and a stress-free bottom boundary and are accurately captured by the scaling prediction (3.8). To validate *a posteriori* the underlying assumptions of the model, we now examine the structure of the boundary layers in the DNS flows.

The structure of the thermal boundary layer is illustrated in figure 2 for a value of the Prandtl number $Pr = 3$ that lies comfortably within the high Prandtl number regime, where a clear departure is observed between no-slip and stress-free bottom boundaries. In this figure, we display the vertical temperature profiles $\bar{\theta}$, where the overline denotes an average along the horizontal directions and over time. Upon examination, the temperature profiles are strikingly similar for no-slip and stress-free cases in the bulk of the flow, while the no-slip case develops strong boundary layers associated with a large temperature jump at the bottom of the layer.
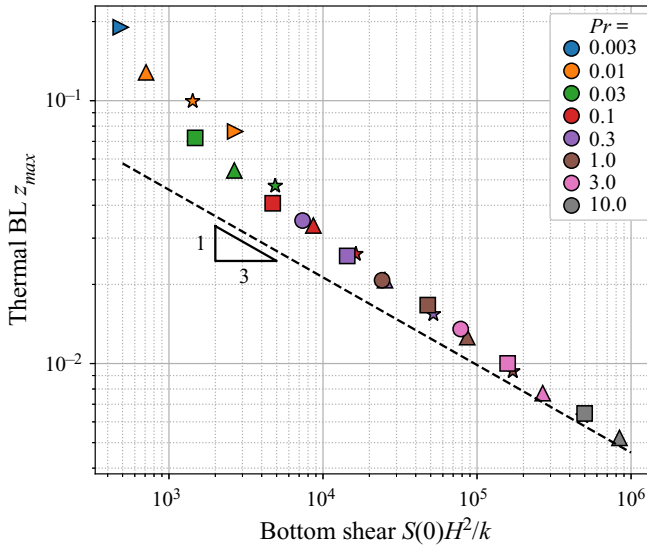
900 R1-8

FIGURE 3. Structure of the boundary layers as Pr and Ra_Q vary. We represent the dimensionless thickness of the thermal boundary layer δ_Θ/H defined as the depth where the diffusive flux is maximum (see figure 2b), represented as a function of the dimensionless shear at the bottom plate $S(0)H^2/\kappa = \overline{\partial_z\sqrt{u^2+v^2}}$. Dashed line: prediction from (3.5).

Beyond the mere temperature profiles, we analyse the thermal energy fluxes in the vicinity of the bottom bounding surface in figure 2(b). For no-slip boundary conditions, the diffusive flux $\overline{\partial_z\theta}(z)$ grows linearly with the distance from the wall z. As a consequence, the diffusive flux strongly dominates the purely convective flux $\overline{w\theta}(z)$, which exhibits a slower quadratic growth with z. As z increases, the diffusive flux reaches a maximum at distance z_{max} and decreases again. Advection and diffusion contribute in equal proportions to the heat transfer at a comparable height z_*, where $\overline{\partial_z\theta}(z_*) = \overline{w\theta}(z_*)$. Above z_* is the bulk, where pure convection proves the most efficient mechanism.

Being able to extract a thermal boundary-layer thickness from the numerical solutions, we now turn our attention to the validity of the sheared boundary-layer assumption (3.5) near a no-slip boundary. The dimensionless bottom shear $S(0)H^2/\kappa$ is estimated as

$$S(0)H^2/\kappa = \overline{\partial_z\sqrt{u^2(x,y,z,t)+v^2(x,y,z,t)}}|_{z=0}. \tag{4.1}$$

The boundary-layer thickness measured by z_{max} is displayed in figure 3 as a function of this dimensionless bottom shear, for all the data gathered with no-slip boundary conditions. A good collapse is observed, and the data for large Prandtl number validate the shear layer structure assumed in (3.5). The approach to this asymptote proves rather slow, because the kinetic boundary layer is only moderately thicker than the thermal one for the highest Pr achieved in this study (approximately 3 times thicker for $Pr = 10$).

4.3. *Boundary-layer structure: stress-free case*

Returning to figure 2(b), the examination of the energy flux profiles in the stress-free case yields a much different scenario. In contrast with the no-slip case, both the convective flux $\overline{w\theta}$ and the diffusive flux $\overline{\partial_z\theta}$ grow linearly with the distance z to the bottom boundary.

900 R1-9

As a first consequence, the ratio between these two fluxes remains asymptotically of $O(1)$ as the distance to the wall decreases. Moreover, energy transfers are dominated by pure convection as $\overline{w\theta} > \overline{\partial_z \theta}$ for any altitude z. All these observations are in strong support of the working hypotheses used for deriving prediction (3.8), and thus shed light on the (non-purely diffusive) nature of the boundary layers that result in the $Nu \sim \sqrt{RaPr}$ scaling observed for all Pr in figure 1.

5. Discussion and conclusion

We have characterised the dimensionless heat flux arising in convection driven by internal heat sources and sinks, focusing on the influence of the diffusivity ratio. Combining the present results with the conclusions of Lepot *et al.* (2018) and Bouillaut *et al.* (2019), we have answered the question raised at the outset – the scaling behaviour of the enhanced heat flux – by proposing the compact scaling relation (3.8) for the Nusselt number. While the scaling exponents appearing in this expression are most likely robust features of CISS, the precise values of the prefactors c_1, c_2 and c_3 may very well depend on details of a given system. For instance, extracting the prefactor c_3 from the experimental data obtained by Lepot *et al.* (2018) in a cylindrical container with a stress-free top boundary leads to approximately 0.9. Their DNS data in a cube with stress-free sidewalls yield a value closer to $c_3 \simeq 1.1$, while the present DNS data with periodic boundary conditions in the horizontal lead to $c_3 \simeq 1.3$.

When a stress-free bottom boundary is considered, we have established that the heat flux follows the standard mixing-length prediction $Nu \sim \sqrt{RaPr}$, both in terms of Rayleigh and Prandtl number. When the bottom boundary condition is no slip, the mixing-length scaling regime is observed at low Prandtl number, $Pr \leq 0.04$. As most astrophysical fluids of interest have a low Prandtl number, this confirms that the associated flows would lead to the mixing-length scaling regime regardless of the bottom boundary condition. The present set-up thus offers a clear realisation of the scaling laws believed to hold in astrophysical contexts.

However, for $Pr > 0.04$ and a no-slip bottom boundary, we find that the stagnant layer in the vicinity of the latter is conducive to a modification of the Prandtl number exponent: $Nu \sim Ra^{1/2} Pr^{1/6}$. This scaling is well captured by modelling the bottom thermal boundary layer as a sheared layer nested inside the kinetic boundary layer. We confirmed this picture through an analysis of the temperature and heat flux profiles extracted from our suite of DNS. This $Pr = O(1)$ situation could be relevant to the atmosphere, in situations where the latter is subject to both infrared heating and cooling (Deardorff 1974). The no-slip bottom boundary and the associated stagnant layer would then crucially impact the temperature profile in the atmospheric boundary layer. But this situation is also relevant to laboratory realisations of CISS (Lepot *et al.* 2018; Bouillaut *et al.* 2019), which use water ($Pr = 7$) together with a no-slip bottom boundary. Several approaches can be envisioned to achieve the $Nu \sim \sqrt{RaPr}$ scaling in such a laboratory experiment. Following the numerical study of Barker *et al.* (2014), one approach would consist in artificially picking a distribution of sources and sinks that vanishes at the top and bottom boundaries, but there is no simple experimental way of tailoring the heat source distribution. A more natural approach from the experimental standpoint would be to use a fluid with a Prandtl number far below $Pr_* = 0.04$, but that again seems rather impracticable. Finally, our study suggests a third and much more promising route towards observing the $Pr^{1/2}$ dependence of the Nusselt number experimentally: tweaking the bottom boundary condition to make it as

close as possible to a stress-free one, by stacking two layers of immiscible fluids, a heavy transparent one below a lighter light-absorbing one.

Acknowledgements

Declaration of interests

The authors report no conflict of interest.

References

AHLERS, G., GROSSMANN, S. & LOHSE, D. 2009 Heat transfer and large scale dynamics in turbulent Rayleigh–Bénard convection. *Rev. Mod. Phys.* **81**, 503–537.

AURNOU, J. M., BERTIN, V., GRANNAN, A. M., HORN, S. & VOGT, T. 2018 Rotating thermal convection in liquid gallium: multi-modal flow, absent steady columns. *J. Fluid Mech.* **846**, 846–876.

AURNOU, J. M., CALKINS, M. A., CHENG, J. S., JULIEN, K., KING, E. M., NIEVES, D., SODERLUND, K. M. & STELLMACH, S. 2015 Rotating convective turbulence in earth and planetary cores. *Phys. Earth Planet. Inter.* **246**, 52–71.

BARKER, A. J., DEMPSEY, A. M. & LITHWICK, Y. 2014 Theory and simulations of rotating convection. *Astrophys. J.* **791** (1), 13.

BOUILLAUT, V., LEPOT, S., AUMAÎTRE, S. & GALLET, B. 2019 Transition to the ultimate regime in a radiatively driven convection experiment. *J. Fluid Mech.* **861**, R5.

BROWNING, M. K 2008 Simulations of dynamo action in fully convective stars. *Astrophys. J.* **676** (2), 1262.

BURNS, K. J., VASIL, G. M., OISHI, J. S., LECOANET, D. & BROWN, B. P. 2020 Dedalus: a flexible framework for numerical simulations with spectral methods. *Phys. Rev. Res.* **2**, 023068.

CALKINS, M. A., JULIEN, K., TOBIAS, S. M. & AURNOU, J. M. 2015 A multiscale dynamo model driven by quasi-geostrophic convection. *J. Fluid Mech.* **780**, 143–166.

CASTAING, B., GUNARATNE, G., HESLOT, F., KADANOFF, L., LIBCHABER, A., THOMAE, S., WU, X.-Z., ZALESKI, S. & ZANETTI, G. 1989 Scaling of hard thermal turbulence in Rayleigh–Bénard convection. *J. Fluid Mech.* **204**, 1–30.

CHAVANNE, X., CHILLÀ, F., CASTAING, B., HÉBRAL, B., CHABAUD, B. & CHAUSSY, J. 1997 Observation of the ultimate regime in Rayleigh–Bénard convection. *Phys. Rev. Lett.* **79**, 3648–3651.

CHILLÀ, F. & SCHUMACHER, J. 2012 New perspectives in turbulent Rayleigh–Bénard convection. *Eur. Phys. J.* E **35** (7), 58.

CIONI, S., CILIBERTO, S. & SOMMERIA, J. 1997 Strongly turbulent Rayleigh–Bénard convection in mercury: comparison with results at moderate Prandtl number. *J. Fluid Mech.* **335**, 111–140.

DEARDORFF, J. W. 1974 Three-dimensional numerical study of the height and mean structure of a heated planetary boundary layer. *Boundary-Layer Meteorol.* **7** (1), 81–106.

DOERING, C. R., TOPPALADODDI, S. & WETTLAUFER, J. S. 2019 Absence of evidence for the ultimate regime in two-dimensional Rayleigh–Bénard convection. *Phys. Rev. Lett.* **123**, 259401.

FAUVE, S, LAROCHE, C & LIBCHABER, A 1981 Effect of a horizontal magnetic field on convective instabilities in mercury. *J. Phys. Lett.* **42** (21), 455–457.

GOLUSKIN, D. 2015 Internally heated convection beneath a poor conductor. *J. Fluid Mech.* **771**, 36–56.

GOLUSKIN, D. & VAN DER POEL, E. P. 2016 Penetrative internally heated convection in two and three dimensions. *J. Fluid Mech.* **791**, R6.

GUERVILLY, C., CARDIN, P. & SCHAEFFER, N. 2019 Turbulent convective length scale in planetary cores. *Nature* **570** (7761), 368–371.

HE, X., FUNFSCHILLING, D., NOBACH, H., BODENSCHATZ, E. & AHLERS, G. 2012 Transition to the ultimate state of turbulent Rayleigh–Bénard convection. *Phys. Rev. Lett.* **108**, 024502.

LEPOT, S., AUMAÎTRE, S. & GALLET, B. 2018 Radiative heating achieves the ultimate regime of thermal convection. *Proc. Natl Acad. Sci. USA* **115** (36), 8937–8941.

MIQUEL, B., LEPOT, S., BOUILLAUT, V. & GALLET, B. 2019 Convection driven by internal heat sources and sinks: heat transport beyond the mixing-length or 'ultimate' scaling regime. *Phys. Rev. Fluids* **4**, 121501.

MIQUEL, B., XIE, J.-H., FEATHERSTONE, N., JULIEN, K. & KNOBLOCH, E. 2018 Equatorially trapped convection in a rapidly rotating shallow shell. *Phys. Rev. Fluids* **3**, 053801.

NIEMELA, J. J., SKRBEK, L., SREENIVASAN, K. R. & DONNELLY, R. J. 2000 Turbulent convection at very high Rayleigh numbers. *Nature* **404** (6780), 837–840.

PLANT, R. S. & YANO, J.-I. 2015 *Parameterization of Atmospheric Convection*. Imperial College Press.

ROCHA, C. B., BOSSY, T., LLEWELLYN SMITH, S. G. & YOUNG, W. R. 2020 Improved bounds on horizontal convection. *J. Fluid Mech.* **883**, A41.

SHISHKINA, O., EMRAN, M. S., GROSSMANN, S. & LOHSE, D. 2017 Scaling relations in large-Prandtl-number natural thermal convection. *Phys. Rev. Fluids* **2**, 103502.

SHISHKINA, O. & WAGNER, S. 2016 Prandtl-number dependence of heat transport in laminar horizontal convection. *Phys. Rev. Lett.* **116**, 024302.

SODERLUND, K. M. 2019 Ocean dynamics of outer solar system satellites. *Geophys. Res. Lett.* **46** (15), 8700–8710.

SODERLUND, K. M., KING, E. M. & AURNOU, J. M. 2012 The influence of magnetic fields in planetary dynamo models. *Earth Planet. Sci. Lett.* **333–334**, 9–20.

SUTHERLAND, B. R., ACHATZ, U., CAULFIELD, C. P. & KLYMAK, J. M. 2019 Recent progress in modeling imbalance in the atmosphere and ocean. *Phys. Rev. Fluids* **4**, 010501.

VREUGDENHIL, C. A., GRIFFITHS, R. W. & GAYEN, B. 2017 Geostrophic and chimney regimes in rotating horizontal convection with imposed heat flux. *J. Fluid Mech.* **823**, 57–99.

YANO, J.-I., TALAGRAND, O. & DROSSARD, P. 2003 Origins of atmospheric zonal winds. *Nature* **421**, 36.